PAPER

Check for updates

Quasi-1D/3D Bi$_2$O$_4$/phase-tuned C$_3$N$_5$ type-II heterostructure for the visible-light-driven photocatalytic degradation of resorcinol in wastewater: insights into the inhibitory effects of matrix interferences and phytotoxicity assessment

Adarsh Singh, [iD] [a] Balbir,[a] Suneel Kumar Srivastava,†[b]
Amit Bhatnagar[c] and Ashok Kumar Gupta [iD] *[a]

Over the years, resorcinol (RCL) has been used to manufacture various pharmaceuticals and personal care products (PPCPs). Its extensive use in treating skin infections has made it ubiquitous in environmental matrices, raising a global threat owing to its endocrine-disrupting nature. In this regard, a novel quasi-1D/3D Bi$_2$O$_4$/PT-C$_3$N$_5$ photocatalyst (referred to as BCN hereafter) was synthesized employing a facile hydrothermal technique for the photocatalytic degradation of RCL. Benefiting from the enhanced visible light responsiveness and impeded charge carrier recombination, the as-fabricated BCN-10 (comprising 10% PT-C$_3$N$_5$) exhibited 94.3% RCL degradation after 180 min under optimal conditions. The BCN-10 photocatalyst was found to be chemically stable and demonstrated reusability up to 5 cycles with a minimal reduction in degradation efficiency. Thereafter, the impact of other emerging contaminants (ECs) and actual water matrices was analyzed to determine the practical applicability of the photocatalytic system. The charge transfer mechanism in BCN-10 was confirmed to follow a type-II pathway, where O$_2$$^{\bullet-}$ and h$^+$ were established as the key reactive species promoting RCL degradation. Furthermore, the seed germination assay performed for treated and untreated RCL solutions showcased a germination index (GI) of 82% indicating the treated RCL solution to be non-phytotoxic. This study helps in understanding the creation of heterojunction photocatalysts by using an emerging non-trivalent variant of bismuth oxide and N-rich phase-tuned graphitic carbon nitride for wastewater treatment.

1. Introduction

Pharmaceuticals and personal care products (PPCPs) are classified as emerging contaminants (ECs), owing to their ability to pose ecological risks, even at low concentrations, adversely affecting both aquatic biota and human health.[1,2] The primary sources of PPCPs in aquatic ecosystems consist of domestic sewage, wastewater treatment plants (WWTPs), agricultural runoff, urban landfills, hospitals, and the pharmaceutical industry.[3–5] PPCPs exhibit resistance to biodegradation owing to their stable chemical structures,

enabling them to bypass conventional WWTPs and persist in receiving waters.[6] The primary concern regarding the presence of PPCPs in aquatic biota is their potential to disrupt the endocrine system and hamper homeostasis.[7] Resorcinol (RCL), also known as 1,3-benzenediol, is a commonly used ingredient in a group of products, such as flame retardants, food additives, and dermal medications.[8–10] In particular, it is used in the formulation of PPCPs applied topically to treat skin conditions such as acne, psoriasis, seborrheic dermatitis, and others.[10] However, there is limited know-how about the environmental persistence of RCL and its possible toxicological effects on non-targeted species compared to other PPCPs. Reportedly, RCL affects the thyroid by inhibiting thyroid peroxidase enzymes, thereby disrupting the synthesis of thyroid hormones.[11] Further, the presence of RCL in drinking water is goitrogenic, as evident from *in vivo* assay in rats.[12] In view of its widespread applications and potential toxicological effects, the removal of RCL from environmental matrices becomes mandatory. To address this

[a] *Environmental Engineering Division, Department of Civil Engineering, Indian Institute of Technology Kharagpur, Kharagpur 721302, India.*
E-mail: agupta@civil.iitkgp.ac.in
[b] *Department of Chemistry, Indian Institute of Technology Kharagpur, Kharagpur 721302, India*
[c] *Department of Separation Science, LUT School of Engineering Science, LUT University, Sammonkatu 12, Mikkeli FI-50130, Finland*
† Retired professor.

issue, advanced oxidation processes (AOPs) have garnered attention as an effective alternative to conventional WWTPs, which are incompetent to adequately remove PPCPs.[13]

As a promising solution, semiconductor-based photocatalysis has gained prominence for the degradation of organic pollutants from aqueous matrices.[14–16] Several metal oxides, comprising ZnO, TiO$_2$, CuO, WO$_3$, and others, have been commonly used for environmental remediation.[17,18] Among these, Bi$_2$O$_3$ has been widely investigated as a photocatalyst owing to its distinct physicochemical properties, such as refractive index, visible light responsiveness, dielectric permittivity, and stability.[19] Recently, the focus has been shifted to another oxide of bismuth, Bi$_2$O$_4$, due to its lower band gap (~2.0 eV) compared to Bi$_2$O$_3$ (~2.8 eV), enabling enhanced visible-light absorption and making it a promising candidate for visible-light-driven photocatalysis.[20,21] Monoclinic Bi$_2$O$_4$, an n-type semiconductor, is a non-trivalent variant of Bi$_2$O$_3$, comprising mixed valence states of Bi(III) and Bi(V).[22] The ability to synthesize Bi$_2$O$_4$ from a single precursor (NaBiO$_3$),[23] without the use of toxic solvents, makes its synthetic route environmentally friendly. However, pristine Bi$_2$O$_4$, like many single-component photocatalysts, suffers from rapid recombination of photoinduced electron (e$^-$) and hole (h$^+$) pairs and photo-corrosion over longer use.[22,24] Hence, it becomes necessary to overcome these drawbacks in order to harness the superior photocatalytic potential of Bi$_2$O$_4$. In this regard, several techniques, such as morphology optimization,[25] defect engineering,[26] heteroatom doping,[27] and heterojunction construction,[28] could be utilized to refine the photocatalytic performance of the semiconducting material. Among these, heterojunction creation is an effective way to improve the separation of photogenerated e$^-$/h$^+$ pairs in Bi$_2$O$_4$, leading to increased photocatalytic efficiency.[26,29–31] Accordingly, several Bi$_2$O$_4$-based heterojunctions have been reported so far, including Bi$_2$O$_3$/Bi$_2$O$_4$,[21] ZnMoO$_4$/Bi$_2$O$_4$,[22] Bi$_2$O$_4$/Fe$_3$O$_4$,[23] and g-C$_3$N$_4$/Bi$_2$O$_4$.[24]

In the last few years, graphitic carbon nitride (g-C$_3$N$_4$) has played a significant role as a metal-free polymeric photocatalyst, owing to its thermal/chemical stability, surface tunability, conductivity, and non-toxicity.[32] Despite these inherent characteristics, g-C$_3$N$_4$ suffers from common limitations like other photocatalysts, including a narrow visible light absorption range, limited active sites for adsorption and catalysis, and accelerated recombination of photoinduced charge carriers.[33,34] The preparation of g-C$_3$N$_4$ using established precursors, including urea,[35] thiourea,[26] and melamine,[36] often causes incomplete polymerization. This leaves non-condensed surface amino moieties that obstruct the migration of charge carriers.[37,38] In addition, high calcination temperatures induce thermal shocks, causing irregular arrangement of homo-triazine units in g-C$_3$N$_4$, which accounts for poor photocatalytic activity.[39] Recent reports show that adding N-rich moieties to the g-C$_3$N$_4$ matrix could decrease the bandgap notably, ascribed to a more extended conjugated framework and the interaction

of N atom lone pairs with the heptazine π system.[40] In this regard, C$_3$N$_5$, with its lower C/N ratio and reduced bandgap (E_g ~ 1.8 eV), has emerged as a viable successor to g-C$_3$N$_4$ (E_g ~ 2.8 eV).[36,40] It is well established that C$_3$N$_5$ exhibits superior opto-electronic characteristics, augmented active sites, and enhanced π–π conjugation in comparison to g-C$_3$N$_4$, attributed to the sp^2-hybridized N in the triazole moiety.[41] Further, the triazine-based carbon nitrides exhibit comparatively inferior photocatalytic efficacy to their heptazine-based counterpart with an elaborate conjugated framework.[42] The π-electron system formed by the heptazine moieties enhances light harvesting, mobility of charge carriers, and stability.[38] Following the aforementioned advantage, Ng *et al.* recently fabricated a phase-tuned C$_3$N$_5$ (PT-C$_3$N$_5$) photocatalyst, comprising both triazine and heptazine phases, using a molten salt-assisted synthesis approach. The material showcased remarkable photocatalytic potential for H$_2$O$_2$ production.[43] This implied that PT-C$_3$N$_5$ can synergistically improve the stability and charge dynamics attributed to the individual properties of the constituting phases. Therefore, it is anticipated that the intrinsic properties of both Bi$_2$O$_4$ and PT-C$_3$N$_5$ could pave the way for the unprecedented creation of a photocatalytic heterostructure with an augmented treatment efficacy for water and wastewater.

Motivated by this rationale, we synthesized a series of novel quasi-1D/3D Bi$_2$O$_4$/PT-C$_3$N$_5$ type-II heterojunction photocatalysts (referred to as BCN hereafter) by varying the weight proportions of PT-C$_3$N$_5$ using the hydrothermal method (Fig. 1). The photocatalytic activity of the as-synthesized photocatalysts was assessed under 50 W LED light using RCL as a model PPCP in water matrices. The physicochemical characteristics of the photocatalysts were analyzed employing various characterization techniques. The degradation efficiency was investigated in relation to a number of operational factors, such as catalyst dose, initial RCL concentration, solution pH, co-existing ions, and natural organic matter (NOM). Furthermore, the impacts of various ECs and real water matrices on RCL degradation were evaluated. Ultimately, radical capturing experiments were performed to ascertain the primary reactive species responsible for RCL degradation, and a plausible degradation mechanism was proposed. Lastly, the *in silico* toxicity of the transformation products (TPs) and the phytotoxicity of the photocatalytically degraded sample were tested.

2. Experimental details

2.1. Chemicals and reagents

The chemicals and reagents used in the present study are detailed in Table S1.

2.2. Synthesis of photocatalysts

2.2.1. Template-free synthesis of N-rich PT-C$_3$N$_5$. A template-free synthesis of N-rich PT-C$_3$N$_5$ was carried out by the thermal polymerization method, as previously reported,
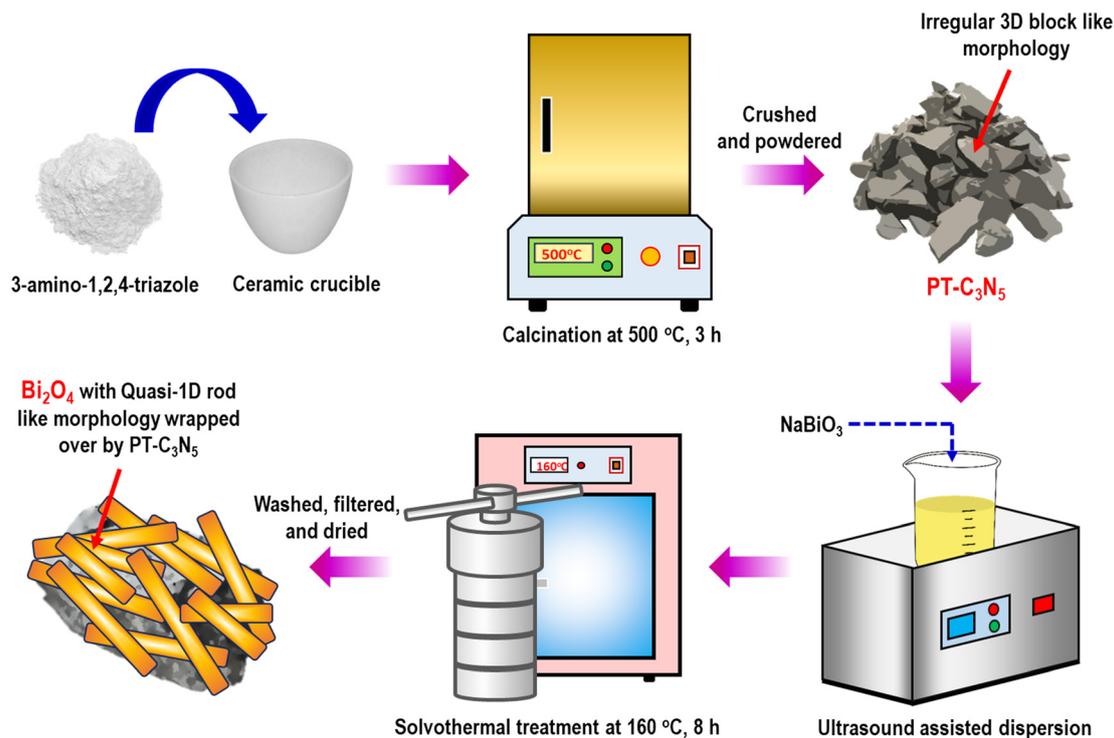
© 2026 The Author(s). Published by the Royal Society of Chemistry

RSC Appl. Interfaces, 2026, **3**, 510–526 | **511**

Fig. 1 Schematic diagram for the preparation of the $Bi_2O_4/PT-C_3N_5$ (BCN) composite.

with minor modifications.[43] In a typical synthesis procedure, 5 g of 3-amino-1,2,4-triazole was placed in a ceramic crucible and calcined for 3 h at 500 °C in a muffle furnace with a heating ramp rate set at 3 °C min^{-1}, and allowed to naturally cool to room temperature. The brownish orange end product (PT-C$_3$N$_5$) so obtained was carefully ground using an agate mortar and pestle.

2.2.2. Synthesis of the $Bi_2O_4/PT-C_3N_5$ heterojunction photocatalyst. Initially, uniform dispersion of PT-C$_3$N$_5$ was obtained by suspending it in 70 mL of DI water and subjecting the contents to ultrasonication for 30 min. Subsequently, 0.56 g of NaBiO$_3$ powder was added to the solution, which was then stirred for 1 h. The so formed yellow solution was then poured to a 100 mL Teflon-lined autoclave reactor and kept in a hot air oven with the temperature set at 160 °C for 8 h. After the reaction period was complete, the bright orange precipitate was filtered out, alternatively cleaned with DI water and ethanol, and subsequently dried overnight at 60 °C. The obtained product was finely ground and labeled as BCN-5, BCN-10, and BCN-20, according to the weight percentages of PT-C$_3$N$_5$ at 5%, 10%, and 20% with respect to NaBiO$_3$. Furthermore, pristine Bi$_2$O$_4$ was also prepared without the addition of PT-C$_3$N$_5$ in a similar manner.[23]

2.3. Analytical techniques and instrumentation

Advanced characterization techniques were employed to examine the physicochemical characteristics of the pristine and composite materials, as numbered in Table S2.

2.4. Assessment of photocatalytic degradation efficiency

A batch-mode photocatalytic reactor was used for assessing the photocatalytic degradation of RCL in a water matrix, as detailed and illustrated in our previous work.[44] It consisted of a box with an inner black surface, enclosing a magnetic stirrer, above which a beaker was placed to hold the reaction mixture. A 50 W LED spotlight ($\lambda \geq$ 420 nm) was fitted at a 10 cm height above the water surface. In a typical experimental protocol, 50 mg of the as-prepared pristine and composite photocatalyst was added to a 50 mL aqueous solution comprising RCL at a concentration of 5 mg L^{-1}. To ensure adsorption–desorption equilibrium between the photocatalyst and the targeted pollutant, the reaction mixture was constantly agitated at 300 rpm for 30 min in the dark before the photocatalytic degradation test. After pre-defined intervals, 3 mL of the suspension was drawn from the reaction mixture, and the photocatalyst slurry was separated using a polyvinylidene difluoride (PVDF) syringe filter (0.2 µm) for analysis. The RCL concentration of the resulting samples was then measured using a Cary 60 UV-vis spectrophotometer at a wavelength of ~272 nm. The extent of RCL degradation was calculated considering the combined effects of adsorption and photocatalysis on RCL degradation in the solution. This synergy significantly enhances the breakdown of organic pollutants. The degradation efficiency (η) was obtained as follows (eqn (1)):

$$\eta \ (\%) = [1 - (C_t/C_0)] \times 100 \tag{1}$$

where C_0 and C_t correspond to the initial concentration of RCL and concentration of RCL at time 't' after exposure to 50 W LED light.

2.5. *In silico* toxicity estimation of the transformation products (TPs)

The ecotoxicity potential of the TPs formed by the photocatalytic breakdown of RCL was assessed using the toxicity estimation software tool (TEST).

2.6. Phytotoxicity assessment of the treated effluent

Vigna radiata seeds were used to assess the phytotoxicity of the photocatalytically degraded RCL solution following the steps outlined in Section S1.

3. Results and discussion

3.1. Characterization of the photocatalyst

3.1.1. Crystal phases and molecular vibrations. The crystal phases of the as-synthesized PT-C$_3$N$_5$, Bi$_2$O$_4$, and BCN-10 photocatalysts were examined using the X-ray diffraction technique. The diffractogram of PT-C$_3$N$_5$, as displayed in Fig. 2a, indicated the presence of both triazine and heptazine phases. The XRD peak observed at $2\theta \sim 12.5°$ corresponds to the periodic repetition of tri-*s* triazine (heptazine (C$_6$N$_7$)) units in the (100) crystal plane.[45,46] In addition, the appearance of the peak at $2\theta \sim 27.0°$ could be ascribed to the (002) inter-layer stacking arrangement of π–π motifs of the heptazine rings.[46,47] The concurrent existence of the triazine phase in PT-C$_3$N$_5$ is confirmed by the diffraction peaks
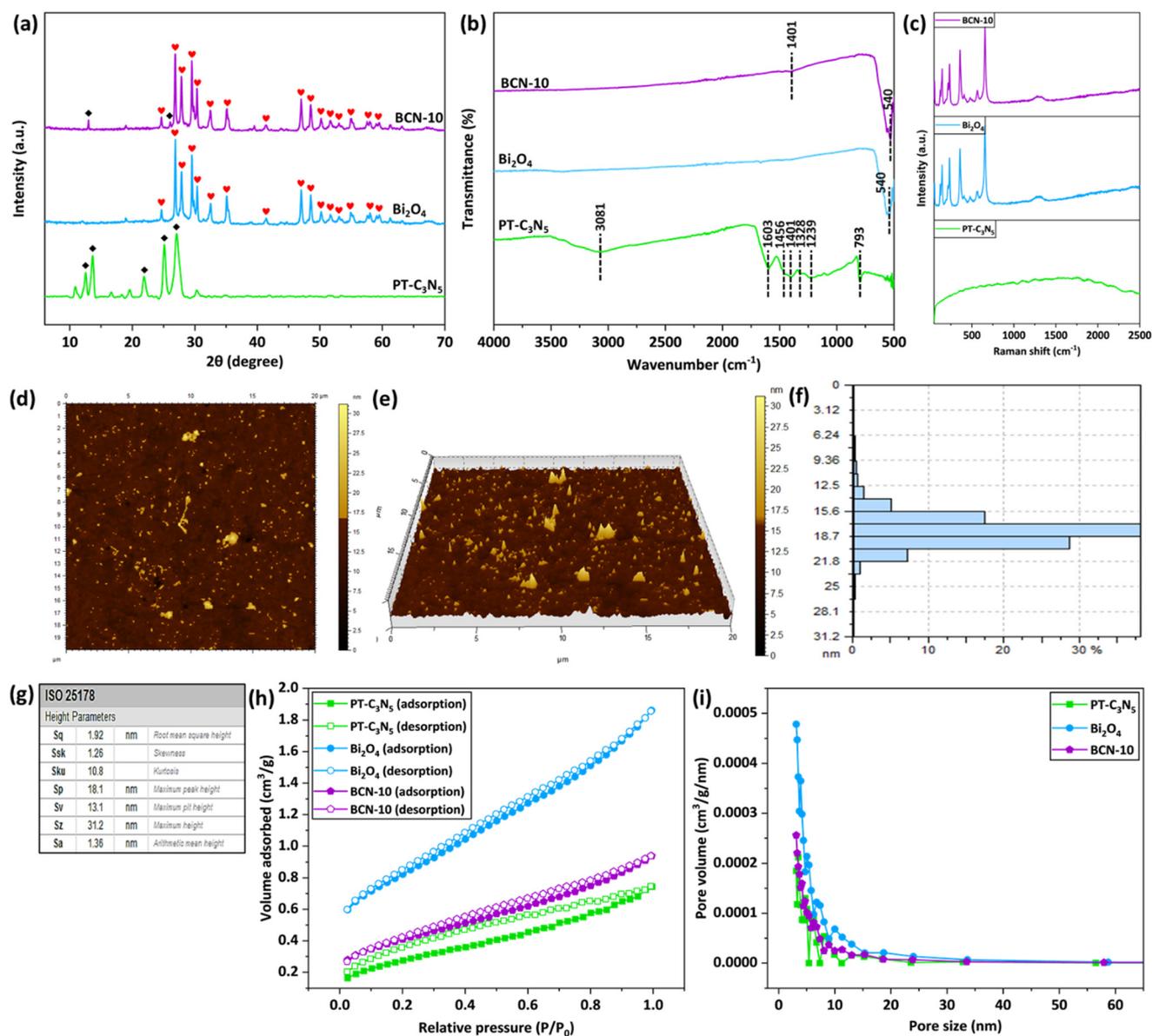

Fig. 2 (a) XRD spectra, (b) FT-IR spectra, and (c) micro-Raman spectra of Bi$_2$O$_4$, PT-C$_3$N$_5$, and BCN-10. (d and e) AFM images, (f) roughness distribution, and (g) height parameters of BCN-10. (h) N$_2$ adsorption–desorption isotherms and (i) pore size distribution of Bi$_2$O$_4$, PT-C$_3$N$_5$, and BCN-10.

observed at $2\theta \sim 13.6°$ and $21.8°$, which correspond to the (001) and (010) crystal planes, respectively, characteristic of the triazine-based carbon nitride. The presence of a subdued peak at $2\theta \sim 25.1°$ in the diffractogram is found to be consistent with the pseudo-stacking pattern of nascent carbon nitride domains (such as oligomers).[48] The major XRD peaks of PT-C_3N_5 are consistent with graphitic carbon nitride and were indexed to JCPDS no. 87-1526 (Fig. S1a). In the context of Bi_2O_4, the major XRD peaks appearing at $2\theta \sim$ $26.9°$, $29.5°$, $30.4°$, $32.5°$, $35.1°$, $47.0°$, and $48.5°$ arise from the (111), (311), (400), (−202), (020), (420) and (−222) facets, respectively, which are in agreement with the monoclinic phase of Bi_2O_4 (m-Bi_2O_4) (JCPDS no. 83-0410, Fig. S1b).[49] The other subdued peaks observed in the spectra were also in agreement with those of m-Bi_2O_4.[49] The XRD pattern of BCN-10 displayed peaks originating from both PT-C_3N_5 and Bi_2O_4 concurrently, suggesting the successful synthesis of the composite.

Fourier-transform infrared (FT-IR) spectroscopy was employed to examine the presence of functional groups and molecular moieties in the as-prepared PT-C_3N_5, Bi_2O_4, and BCN-10 materials (Fig. 2b). In the FT-IR spectrum of PT-C_3N_5, a distinctive absorption peak at 793 cm^{-1} corresponds to the bending vibrations of the triazine rings, while the peak at 1401 cm^{-1} is attributed to the C–N stretching vibrations of the heptazine rings.[50] The appearance of a peak at 1456 cm^{-1} could be related to the C–H bond deformations.[51] In addition, the absorption peaks at 1603 cm^{-1}, 1328 cm^{-1}, and 1239 cm^{-1} could be related to the stretching vibrations of the C=N, C–N, and C–NH–C groups, respectively.[52–54] The broad peak centered at 3081 cm^{-1} can be associated with the stretching vibrations of the N–H bonds.[55] The FT-IR spectrum of Bi_2O_4 showed an intense absorption peak at 540 cm^{-1}, which aligns with the Bi–O bond vibration in distorted BiO_6 units.[56] In the context of BCN-10, a subdued peak at 1401 cm^{-1} from PT-C_3N_5, alongside the peak of Bi_2O_4 at 540 cm^{-1}, confirmed the successful synthesis of the composite.

The micro-Raman spectra of PT-C_3N_5, Bi_2O_4, and BCN-10 were also recorded, and the findings are displayed in Fig. 2c. As evident from the micro-Raman spectrum of PT-C_3N_5, the two broad peaks concentrated at 1566 cm^{-1} and 1372 cm^{-1} can be linked to the G and D bands of graphitic carbon nitride, respectively.[57] In the case of Bi_2O_4, the vibrations involving the translational movements of Bi^{3+} ions are responsible for the strong band at 145 cm^{-1}.[58] The absorption band at $\sim$359 cm^{-1}, due to its prominence, can be associated with the Bi–O–Bi vibrational mode.[59] The other two absorption bands at 234 cm^{-1} and 655 cm^{-1} could be assigned to Bi–O rocking vibrations.[60,61] The Raman peaks in BCN-10 remain more or less unaltered *vis-à-vis* Bi_2O_4 due to the weaker Raman signals of PT-C_3N_5 and its lower amount in the composite.

3.1.2. Topographical features and textural properties. The surface architectural profile of the BCN-10 composite has been studied using atomic force microscopy (AFM). The corresponding AFM images of BCN-10 displayed in

Fig. 2d and e demonstrated a rough surface characterized by surface irregularities distributed throughout the sample. The AFM height profile and associated parameters, as depicted in Fig. 2f and g, showed that the height of the BCN-10 particles varied in the range of $\sim$6 nm and $\sim$26 nm, with root mean square height (Sq) and arithmetic mean height (Sa) as 1.92 nm and 1.36 nm, respectively. The BCN-10 surface features more protrusions than depressions, as confirmed by a positive surface skewness (Ssk) of 1.26. In addition, a surface kurtosis (Sku) of 10.8 indicated the peakedness of the BCN-10 surface. This will most likely affect the surface wettability of BCN-10 and contribute towards its enhanced photocatalytic activity.

Furthermore, the specific surface area (SSA) and pore size distribution of the as-prepared photocatalysts have been determined using the N_2 adsorption–desorption analysis, and the corresponding findings are shown in Fig. 2h and i. Based on this, the BET surface areas of Bi_2O_4, PT-C_3N_5, and BCN-10 were found to be 2.865, 1.034, and 1.469 m^2 g^{-1}, respectively. As presented in Fig. 2h, the aforementioned materials demonstrate a typical type IV isotherm with an H3 hysteresis loop, displaying the presence of mesoporosity. In addition, the pore size distribution of Bi_2O_4, PT-C_3N_5, and BCN-10 is depicted in Fig. 2i and described in Table S3. The SSA of the BCN-10 composite was found to be lower than that of pristine Bi_2O_4, suggesting that SSA is not the only factor influencing the photocatalytic efficacy of the material.[62]

3.1.3. Morphology and elemental composition. The morphology of the as-prepared materials was studied through field emission gun scanning electron microscopy (FEG-SEM) and high-resolution transmission electron microscopy (HR-TEM), and corresponding findings are displayed in Fig. 3 and 4. It is observed that the pristine Bi_2O_4 exhibits a quasi-1D rod-like structure (Fig. 3a), characterized by a smooth surface and extending up to 0.5–2.8 μm (Fig. S2a). Fig. 3b presents a 3D blocky structure of PT-C_3N_5, formed through a stacked sheet-like arrangement, with sizes ranging from about 5 to 35 μm (Fig. S2b). The FEG-SEM image of BCN-10 revealed a distinct structure, where observable Bi_2O_4 micro-rods were fully wrapped around PT-C_3N_5 blocks (Fig. 3c). In addition, energy dispersive spectroscopy (EDS) investigation of BCN-10, as depicted in Fig. 3d, and related elemental mapping (Fig. 3e) established the co-occurrence of Bi, O, C, and N in BCN-10.

To further affirm the creation of quasi-1D/3D heterogeneous structure between Bi_2O_4 and PT-C_3N_5, the TEM images of the BCN-10 composite were recorded, and are presented in Fig. 4a and b. The Bi_2O_4 quasi-rods were observed to be more or less uniformly dispersed on the surface of PT-C_3N_5 blocks. Moreover, the presence of a two-directional interwoven lattice in Fig. 4c indicates strong interaction between the constituting materials in BCN-10. The fast Fourier transformation (FFT) analysis untangled the lattices pertaining to Bi_2O_4 and PT-C_3N_5 (Fig. 4d and e). The measured d-spacing of 0.332 nm and 0.351 nm could be
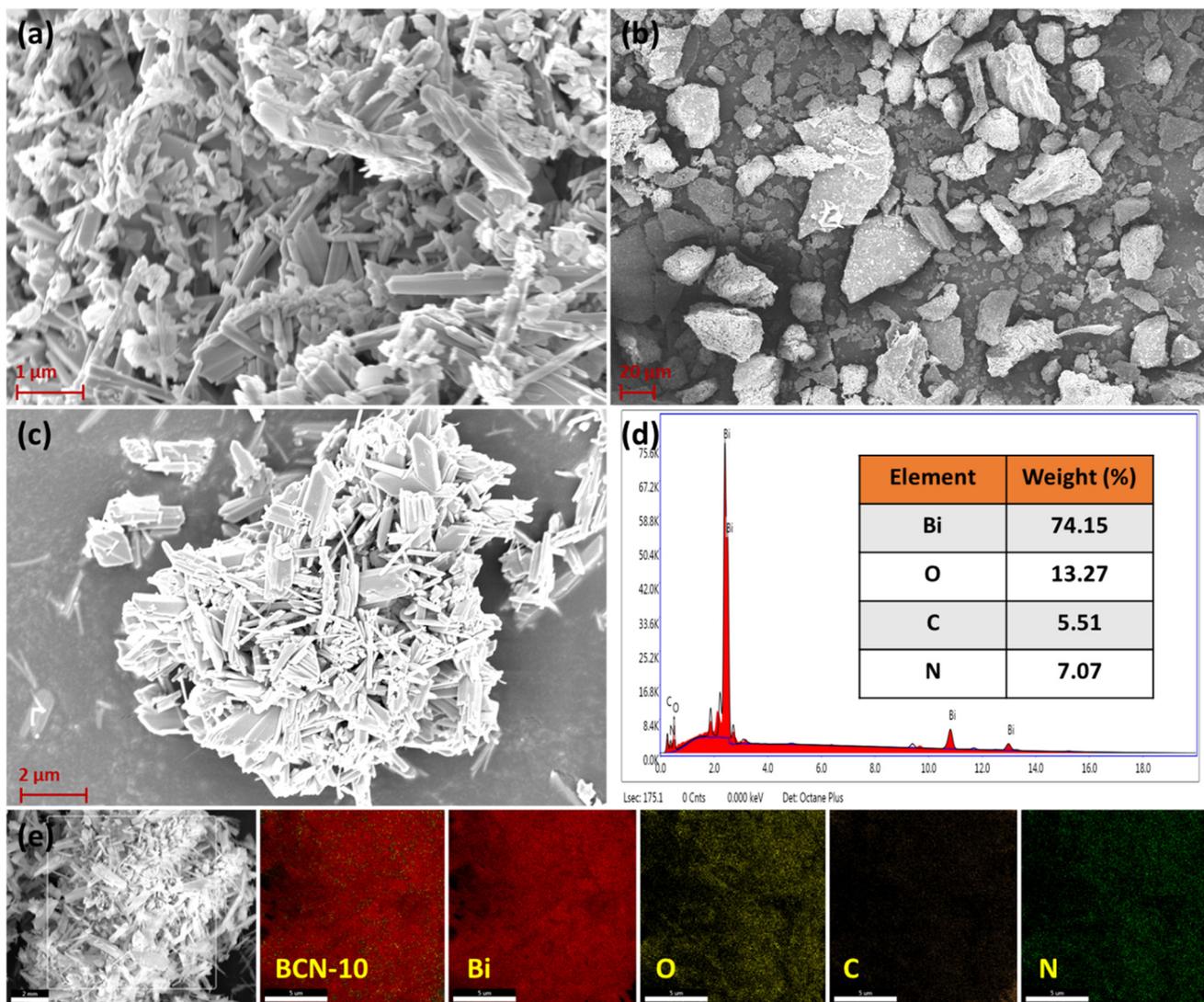
Fig. 3 FEG-SEM images of (a) Bi_2O_4, (b) $PT-C_3N_5$, and (c) BCN-10. (d) EDS spectrum and (e) corresponding elemental mapping of BCN-10.

ascribed to the (111) crystal planes of Bi_2O_4,[63] and graphitic PT-C_3N_5,[64] respectively. In addition, the selected area electron diffraction (SAED) pattern of BCN-10 showed the presence of bright spots arranged in concentric rings, thereby indicating the formation of the polycrystalline material (Fig. 4f).

X-ray photoelectron spectroscopy (XPS) was used to analyze the chemical environment of the elements constituting BCN-10. The peaks related to Bi, O, C, and N can be observed from the full scan survey spectrum of BCN-10 (Fig. 5a). As displayed in Fig. 5b, the high-resolution Bi 4f XPS spectrum exhibits two sets of spin–orbit doublets. For pristine Bi_2O_4, the peaks at 162.8 eV (Bi $4f_{5/2}$) and 157.5 eV (Bi $4f_{7/2}$) correspond to the trivalent oxidation state of Bi (Fig. S3).[65] In the case of BCN-10, these peaks are observed with a slight shift to 162.1 eV and 156.8 eV, respectively (Fig. 5b), indicating an interaction between PT-C_3N_5 and Bi_2O_4. In addition, the other set of spin–orbit doublets at 163.3 eV and 158.1 eV was attributed to the presence of Bi^0 species, corresponding to metallic Bi.[66] The high-resolution XPS

spectrum of O 1s was deconvoluted into two peaks at 527.5 eV and 529.2 eV, which could be associated with the lattice oxygen and adsorbed oxygen species, respectively (Fig. 5c).[67,68] The two peaks in the C 1s spectrum (Fig. 5d), appearing at 285.3 eV and 282.9 eV, could be assigned to the sp^3 C–C and sp^2 C=C bonds.[69,70] Moreover, the peak at 283.6 eV corresponds to the C–O–C or C–O bonds.[71] Furthermore, the dominant peak centered at 397.8 eV in the N 1s spectrum can be linked to the sp^2 hybridized N atoms (N–C=N) in triazine rings (Fig. 5e).[72] The peak observed at 399.6 eV can be related to the linking N atoms in N–$(C)_3$ groups.[73] Additionally, the subdued peak at 396.3 eV corresponds to the sp^2 C–N–C bonds.[74] The full survey scan spectra and high-resolution XPS spectra of pristine Bi_2O_4 and PT-C_3N_5 are displayed in Fig. S3. The peaks corresponding to the constituent elements from the pristine materials in BCN-10 indicate the successful formation of the composite.

3.1.4. Photo-absorption properties. The UV-vis diffuse reflectance spectra (UV-DRS) of the as-fabricated
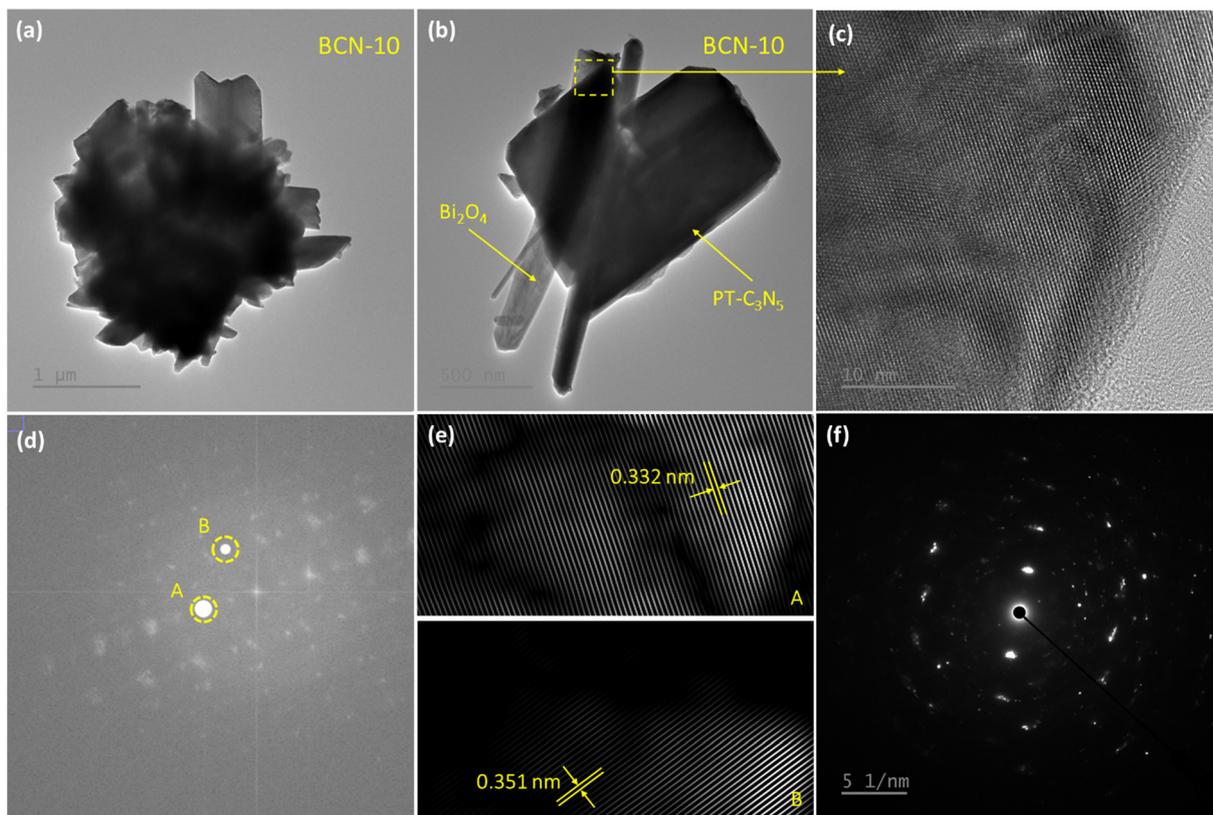
Fig. 4 (a and b) TEM images and (c) HR-TEM images of BCN-10. (d) FFT image of BCN-10 depicting two bright spots A and B (points selected through fill option) corresponding to Bi_2O_4 and $PT\text{-}C_3N_5$, (e) inverse FFT image showing lattice distances, and (f) SAED pattern of BCN-10.
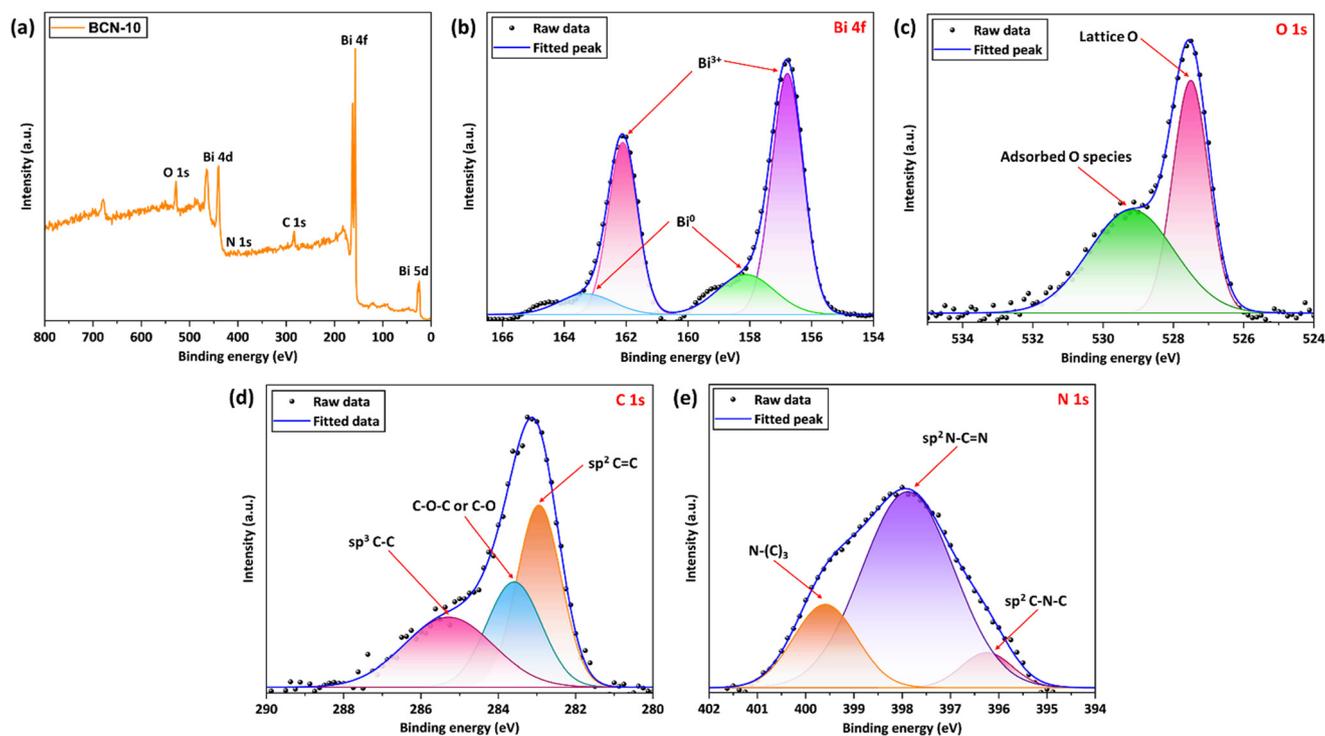

Fig. 5 (a) Full survey scan XPS spectrum of BCN-10. High resolution XPS spectrum of (b) Bi 4f, (c) O 1s, (d) C 1s, and (e) N 1s.
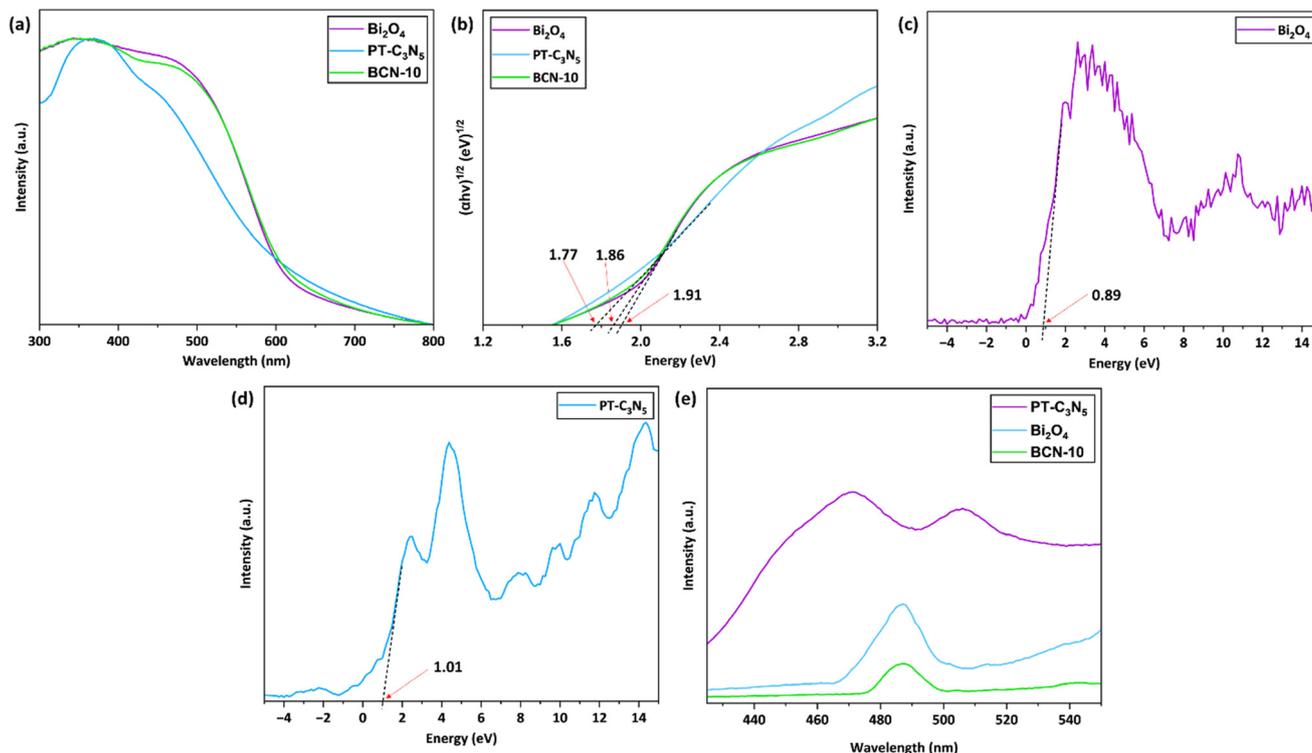
Fig. 6 (a) UV-vis DRS spectra and (b) Tauc plots of Bi_2O_4, $PT-C_3N_5$, and BCN-10. XPS VB spectra of (c) Bi_2O_4 and (d) $PT-C_3N_5$. (e) PL spectra of $PT-C_3N_5$, Bi_2O_4, and BCN-10.

photocatalysts are displayed in Fig. 6a. The absorption onsets of Bi_2O_4, $PT-C_3N_5$, and BCN-10 extended beyond 600 nm in the visible light region. BCN-10 demonstrated a slight blue shift in comparison to pristine Bi_2O_4, due to the enhanced visible light responsiveness. Fig. 6b presents the Tauc plots of Bi_2O_4, $PT-C_3N_5$, and BCN-10, as described by the Kubelka–Munk function (eqn (2)).[75]

$$\alpha h v = A(h v - E_g)^{n/2} \qquad (2)$$

where α, $h v$, E_g, and A correspond to the coefficient of absorption, photon energy, energy band gap, and constant of proportionality, respectively. Moreover, the kind of transition (direct or indirect) associated with the light-absorption process determines the value of n. The E_g values were calculated using eqn (2), and followed the sequence: Bi_2O_4 (1.91 eV) > BCN-10 (1.86 eV) > $PT-C_3N_5$ (1.77 eV). These findings clearly demonstrated that the reduced E_g of BCN-10 improved its absorption for a wider range of visible light and accounted for its superior performance as a photocatalyst. Further, Fig. 6c and d display the XPS-VB spectra of Bi_2O_4 and $PT-C_3N_5$, presenting their respective VB potentials (E_{VB}) as +0.89 eV and +1.01 eV. Utilizing E_{VB} and E_g for Bi_2O_4 and $PT-C_3N_5$, their CB potentials (E_{CB}) can be obtained as follows (eqn (3)):

$$E_{CB} = E_{VB} - E_g \qquad (3)$$

Accordingly, the E_{CB} values for Bi_2O_4 and $PT-C_3N_5$ were calculated and found to be −1.02 eV and −0.76 eV, respectively. Furthermore, the photoluminescence (PL) spectra of all as-fabricated photocatalysts have also been recorded and are presented in Fig. 6e. These findings revealed the decrease in the PL intensity of BCN-10, in comparison to Bi_2O_4 and $PT-C_3N_5$. This implied the creation of a heterojunction at the interface of Bi_2O_4 and $PT-C_3N_5$, which advantageously prevented the recombination of photoproduced charge carriers. Furthermore, Fig. S4 displays the findings of electrochemical impedance spectroscopy (EIS) of the as-synthesized $PT-C_3N_5$, Bi_2O_4, and BCN-10. The smallest Nyquist plot radius of BCN-10 implies that it provides the least resistance to charge transfer compared to the other pristine materials.[76]

3.2. Photocatalytic performance of the synthesized photocatalyst

In order to optimize the proportion of $PT-C_3N_5$ in the BCN composites, the photocatalysts (Bi_2O_4, $PT-C_3N_5$, and BCN composites) were tested for RCL degradation in an aqueous solution under 50 W LED light (catalyst dose: 1 g L^{-1}, initial RCL concentration: 5 mg L^{-1}, pH: 7, temperature: 27 ± 2 °C) (Fig. 7a). Subsequently, the optimal $PT-C_3N_5$ content in the BCN composite was determined to be 10%, demonstrating the highest degradation efficiency of 94.3% after 180 min. The
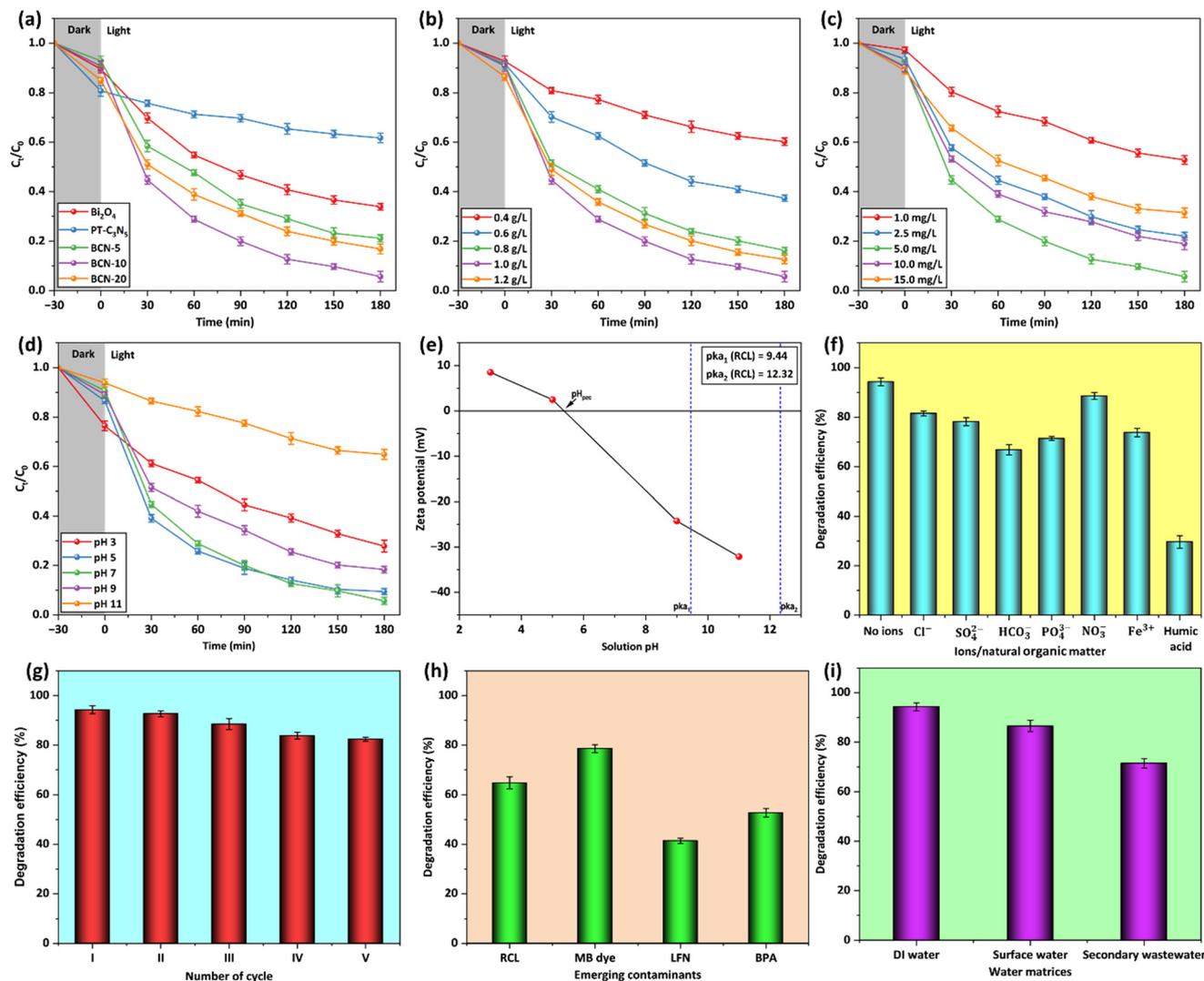
Fig. 7 Photocatalytic degradation of RCL over (a) as-prepared photocatalysts exposed to 50 W LED light after a reaction time of 180 min (BCN-10 dose: 1 g L^{-1}, initial RCL concentration: 5 mg L^{-1}, pH: 7, and temperature: 27 ± 2 °C). Influence of (b) BCN-10 dose (initial RCL concentration: 5 mg L^{-1}, pH: 7, and temperature: 27 ± 2 °C), (c) initial RCL concentration (BCN-10 dose: 1 g L^{-1}, pH: 7, and temperature: 27 ± 2 °C), and (d) solution pH (BCN-10 dose: 1 g L^{-1}, initial RCL concentration: 5 mg L^{-1}, and temperature: 27 ± 2 °C), on RCL degradation. (e) pH-dependent surface charge profile of BCN-10. (f) Influence of inorganic ions and humic acid on RCL degradation. (g) Reusability study of the BCN-10 composite. (h) Influence of different emerging contaminants and (i) various water matrices on RCL degradation.

photocatalytic performance of BCN-10 was notably superior compared to Bi$_2$O$_4$ (66.1%) and PT-C$_3$N$_5$ (38.3%) due to the synergistic effect of the constituting photocatalysts and effective charge separation. Moreover, Bi$_2$O$_4$, PT-C$_3$N$_5$, BCN-5, BCN-10, and BCN-20 composites exhibited controlled adsorption of 10.5%, 19.2%, 7.2%, 9.3%, and 15.0%, respectively, after a 30 min dark period (Fig. S5). Unlike the PT-C$_3$N$_5$ variation from 5% to 10% in the BCN composite, any further increase beyond 10% caused a notable decline in RCL degradation, which can be linked to the excess PT-C$_3$N$_5$ covering the reactive sites and obstructing the migration of charge carriers.

Further, RCL photocatalytic degradation satisfactorily adheres to the Langmuir–Hinshelwood model depicting pseudo-first-order reaction kinetics (eqn (4)):[77]

$$-\ln\left(\frac{C_t}{C_0}\right) = kt \qquad (4)$$

where k is the degradation rate constant and C_t and C_0 are the RCL concentration at any time t and $t = 0$, respectively. It was observed that BCN-10 showcased the maximum rate of degradation ($k = 0.0145$ min^{-1}), about 9.67 and 2.68 times that of PT-C$_3$N$_5$ ($k = 0.0015$ min^{-1}) and Bi$_2$O$_4$ ($k = 0.0054$ min^{-1}), respectively, as shown in Fig. S6. The degradation efficiency of BCN-10 for RCL degradation in the present study was compared with that obtained using previously reported photocatalysts (Table S4).
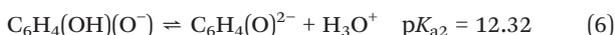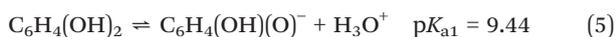
3.2.1. Impact of operational factors on RCL degradation

3.2.1.1. Impact of BCN-10 dosage on RCL degradation. The effect of BCN-10 dosages (0.4 g L^{-1} to 1.2 g L^{-1}) on RCL

degradation was determined, while maintaining other parameters constant (initial RCL concentration: 5 mg L^{-1}, solution pH: 7, temperature: 27 ± 2 °C) (Fig. 7b). It was noted that the visible light exposure of 180 min resulted in the enhanced RCL degradation from 39.8% to 94.3%, with increasing BCN-10 dose from 0.4 g L^{-1} to 1 g L^{-1}, respectively. This could be ascribed to the augmented number of reactive sites with the rise in the photocatalyst dosage.[78] Further increasing the catalyst dose caused a decline in the degradation efficiency (~87%), possibly due to the shielding of the reactive sites on the photocatalyst's surface, due to the agglomeration of the BCN-10 particles.[79] In addition, a higher catalyst dose would make the solution turbid, which would impair the light transmittance and, hence, the production of charge carriers. The results showed 1 g L^{-1} as the optimum catalyst dose for maximum RCL degradation, with the highest k value of 0.0145 min^{-1}.

3.2.1.2. Impact of initial RCL concentration on RCL degradation. The RCL concentration was increased from 1 mg L^{-1} to 15 mg L^{-1} to assess its effect on the photocatalytic degradation of RCL, keeping other parameters constant (BCN-10 dose: 1 g L^{-1}, solution pH: 7, temperature: 27 ± 2 °C) (Fig. 7c). The degradation efficacy improved from 47.2% to 94.3% as the RCL concentration increased from 1 mg L^{-1} to 5 mg L^{-1} due to the enhanced interaction between RCL molecules and BCN-10 particles.[80] Further, upon increasing RCL concentration from 5 mg L^{-1} to 10 mg L^{-1}, a notable decline was observed (~13%), likely due to light absorption by RCL molecules, limiting light transmission to the BCN-10 surface. Correspondingly, the k value decreased from 0.0145 min^{-1} to 0.0081 min^{-1} as the RCL concentration increased from 5 mg L^{-1} to 10 mg L^{-1}. The elevated pollutant concentrations reportedly hinder photon migration to the photocatalyst surface, limiting charge carrier generation and reducing degradation efficiency.[81] At lower RCL concentrations, active sites on the surface of the catalyst are abundant but become insufficient as RCL concentration exceeds a certain limit (>5 mg L^{-1}).[82] Hence, 5 mg L^{-1} of RCL concentration was found to be optimum for reaching maximum degradation of RCL.

3.2.1.3. Impact of the solution pH on RCL degradation. The effect of the solution pH on RCL degradation was analyzed, taking into account the pH-dependent ionization state of RCL and the BCN-10 surface charge characteristics (Fig. 7d). The pH of the solution for this purpose was adjusted from 3 to 11 by adding 0.1 M HCl or 0.5 M NaOH. As per the literature, the pH-dependent dissociation profile of RCL can be described as follows (eqn (5) and (6)):[83]

$$C_6H_4(OH)_2 \rightleftharpoons C_6H_4(OH)(O)^- + H_3O^+ \quad pK_{a1} = 9.44 \quad (5)$$

$$C_6H_4(OH)(O^-) \rightleftharpoons C_6H_4(O)^{2-} + H_3O^+ \quad pK_{a2} = 12.32 \quad (6)$$

As mentioned above, at pH > pK_{a1}, RCL predominantly exists in its negatively charged forms as the resorcinate monoanion (C$_6$H$_4$(OH)(O)$^-$) and dianion (C$_6$H$_4$(O)$^{2-}$). Conversely, at pH <

pK_{a1}, RCL remains in its neutral form (C$_6$H$_4$(OH)$_2$). Moreover, Fig. 7e shows the surface charge profile of BCN-10, following the zeta potential measurements. It is inferred that the positively charged surface of BCN-10 neither attracts nor repels the neutral RCL molecule under lower pH conditions. In contrast, the abundant H$^+$ ions in the acidic environment reduce the availability of O$_2$$^{\cdot-}$ radicals,[84] mainly responsible for RCL degradation. As a result, reducing the pH from 5 to 3 decreases the RCL degradation efficacy from 90.5% to 72.1%. Furthermore, at pH ≥ 9, the increasing electrostatic repulsion between the negatively charged surface of BCN-10 and resorcinate anions notably reduces the photocatalytic degradation of RCL to 35.1% (at pH 11), with the least degradation rate (0.0021 min^{-1}). Further, the maximum RCL degradation (94.3%) recorded at pH 7 could be ascribed to the absence of electrostatic repulsion and the increased availability of O$_2$$^{\cdot-}$ species, facilitating efficient RCL degradation. Therefore, pH 7 was found to be optimal for the effective degradation of RCL.

3.2.1.4. Impact of inorganic ions and humic acid on RCL degradation. The photocatalytic degradation of organic contaminants is hindered by the existence of inorganic ions and natural organic matter (NOM). Hence, quantification of their impact is necessary. Various inorganic ions, including Cl$^-$, SO$_4$$^{2-}$, HCO$_3$$^-$, PO$_4$$^{3-}$, NO$_3$$^-$, and Fe^{3+}, were added at a concentration of 100 mg L^{-1} to the reaction mixture (Fig. 7f). The photocatalytic degradation of RCL was compromised by Cl$^-$ ions due to their competitive adsorption on the catalytic sites against RCL molecules. Additionally, Cl$^-$ ions could consume h$^+$, responsible for RCL degradation.[85] Likewise, SO$_4$$^{2-}$ could be adsorbed on the photocatalyst surface, interfering with h$^+$ and forming SO$_4$$^{\cdot-}$, which is less reactive due to its size and resonance effect.[86] It was also observed that NO$_3$$^-$ ions exerted minimal influence on the RCL degradation, due to their low reactivity. The impact of HCO$_3$$^-$ ions was most pronounced, which reduced RCL degradation to 66.8%, which could be supported by the fact that HCO$_3$$^-$ ions react with O$_2$$^{\cdot-}$ generating HCO$_3$$^{\cdot-}$ and CO$_3$$^{\cdot-}$ ions with lower oxidizing potential.[87,88] The photocatalytic degradation of RCL was inhibited in the presence of PO$_4$$^{3-}$ ions due to its acidic behavior and strong binding affinity towards catalytic sites.[29] In the reaction mixture, Fe^{3+} ions tend to form an Fe(OH)$_2$$^+$ complex, which absorbs a portion of the incident irradiation, thus limiting the photocatalysis of RCL to 73.8%.[89] Humic acid was also introduced in the reaction mixture, representing NOM in surface water. Consequently, the RCL degradation declined to 29.6%, caused by the competitive adsorption and radical scavenging ability of humic acid.[90]

3.3. Mineralization efficiency of BCN-10

The mineralization ability of BCN-10 was analyzed using total organic carbon (TOC) measurement, and findings are displayed in Fig. S7. The TOC removal efficiency was determined to be 62.5% after 180 min. This suggests that

© 2026 The Author(s). Published by the Royal Society of Chemistry

RSC Appl. Interfaces, 2026, **3**, 510–526 | 519

RCL molecules break down first, followed by the mineralization of TPs over an extended period of time.

3.4. Stability and reusability potential of BCN-10

The chemical stability of BCN-10 was assessed by quantifying the Bi leaching in the reaction mixture using inductively coupled plasma mass spectrometry (ICP-MS). The concentration of Bi detected in the treated effluent was negligible, indicating BCN-10 to be chemically stable. As depicted in Fig. 7g, around 12% drop in RCL degradation was observed when the BCN-10 photocatalyst was repeatedly used for up to 5 cycles. After each cycle, the photocatalyst was separated through centrifugation, followed by filtration, repeated washing with ethanol and DI water, and finally dried at 60 °C for 12 h. The observed decrement in degradation efficacy can be linked to the remaining adsorbed RCL molecules anchored to the BCN-10 surface. Moreover, the possibility of BCN-10 agglomeration during repeated cycles of use cannot be excluded. The structural stability of BCN-10 was not compromised, as evidenced by the XRD pattern of the spent BCN-10 photocatalyst, which remained intact and closely resembled that of the pristine BCN-10 (Fig. S8). However, minor shifts observed in the XPS peaks of the constituent elements indicate subtle changes in the local chemical environment, likely resulting from the residual RCL molecules remaining adsorbed onto the photocatalyst surface during repeated use (Fig. S9).

3.5. Influence of other ECs and real water matrices

Investigating the influence of environmentally prevalent ECs becomes necessary due to their adverse impact on the photocatalytic degradation of RCL. In this regard, Fig. 7h depicts the degradation of RCL considering the influence of different ECs (each at a concentration of 5 mg L^{-1}), such as an organic dye (*i.e.*, methylene blue (MB)), a pharmaceutical (*i.e.*, levofloxacin (LFN)), and a plasticizer (*i.e.*, bisphenol A (BPA)), by introducing them into the solution along with RCL. These studies showed that the RCL degradation declined to 64.8% due to the competitive interaction of other ECs with active catalytic sites on the BCN-10 surface and the concurrent consumption of radicals that would otherwise solely contribute to RCL degradation. The degradation efficiencies of BCN-10 for MB, LFN, and BPA were found to be 78.6%, 41.4%, and 52.7%, respectively. Furthermore, the practical applicability of BCN-10 was investigated in various real water matrices, including DI water, surface water, and secondary effluent. The water quality parameters of the aforesaid water matrices are recorded in Table S5. As presented in Fig. 7i, a minimal reduction in RCL degradation was observed in surface water (86.5%) compared to DI water (94.3%), possibly due to the induced turbidity and the minimal presence of inorganic ions. This inhibition became more pronounced in the secondary effluent, where increased turbidity, total suspended solids (TSS), and a higher concentration of organic content and inorganic ions resulted in decreased degradation efficiency (71.4%). Therefore, it has been suggested that the pre-treatment would help to reduce the interferences that could otherwise inhibit the efficacy of the photocatalytic treatment system.[91,92] The constituents of the respective water matrices led to the consumption of reactive species, shielding of catalytic sites, and reduced light transmittance, and accounted for the observed inhibited degradation of RCL.

3.6. Photocatalytic mechanism for RCL degradation

A radical scavenging study was performed to recognize the key active species playing a crucial role in RCL degradation (Fig. 8a). The typical experimental procedure involved radical scavengers (each at a concentration of 1 mM), comprising ascorbic acid (ASA), potassium iodide (KI), and isopropyl alcohol (IPA) that were individually introduced in the reaction mixture to capture $O_2^{\cdot-}$, h^+, and $\cdot OH$, respectively. These findings indicated that ASA, among all scavengers, contributed to the most detrimental effect on RCL degradation, reducing the degradation efficiency to 28.4%. This implied $O_2^{\cdot-}$ to be the main active species governing the photocatalytic degradation of RCL. In the existence of KI, RCL degradation declined to 59.2%, signifying the role of h^+ to be secondary. Unlike ASA and KI, IPA had a negligible impact on the RCL degradation efficacy. The predominance of $O_2^{\cdot-}$ in RCL degradation, as stated earlier, was ascertained by electron paramagnetic resonance (EPR) spectroscopy (Fig. 8b).

Based on the as-obtained E_g, E_{CB}, and E_{VB} values, a charge transfer mechanism for BCN-10 can be proposed, as illustrated in Fig. 8c. Pristine Bi_2O_4 and PT-C_3N_5 make BCN-10 generate e^- and h^+ pairs in their respective CB and VB when exposed to LED light. It is anticipated that electrons (e^-) in the CB of Bi_2O_4 (E_{CB} = −1.02 eV) migrate to the less negative CB of PT-C_3N_5 (E_{CB} = −0.76 eV), and holes (h^+) in the VB of PT-C_3N_5 (E_{VB} = +1.01 eV) migrate to the less positive VB of Bi_2O_4 (E_{VB} = +0.89 eV). The e^- in the CB of PT-C_3N_5 could react with O_2 in the reaction mixture to produce $O_2^{\cdot-}$, due to the lower redox potential of $O_2/O_2^{\cdot-}$ (−0.33 eV NHE^{-1}).[93] In contrast, the redox potentials of $OH^-/\cdot OH$ (+1.99 eV NHE^{-1}) and $H_2O/\cdot OH$ (+2.38 eV NHE^{-1}) are notably higher than the VBs of Bi_2O_4 and PT-C_3N_5, making h^+ incompetent to generate $\cdot OH$ radicals.[94] The aforementioned results suggest that Bi_2O_4 and PT-C_3N_5 form a type-II heterojunction in the BCN-10 composite.

3.7. Transformation products (TPs) and *in silico* toxicity investigation

The photocatalytic degradation of RCL proceeded through various degradation pathways, resulting in the formation of various TPs and leading to mineralization into CO_2 and
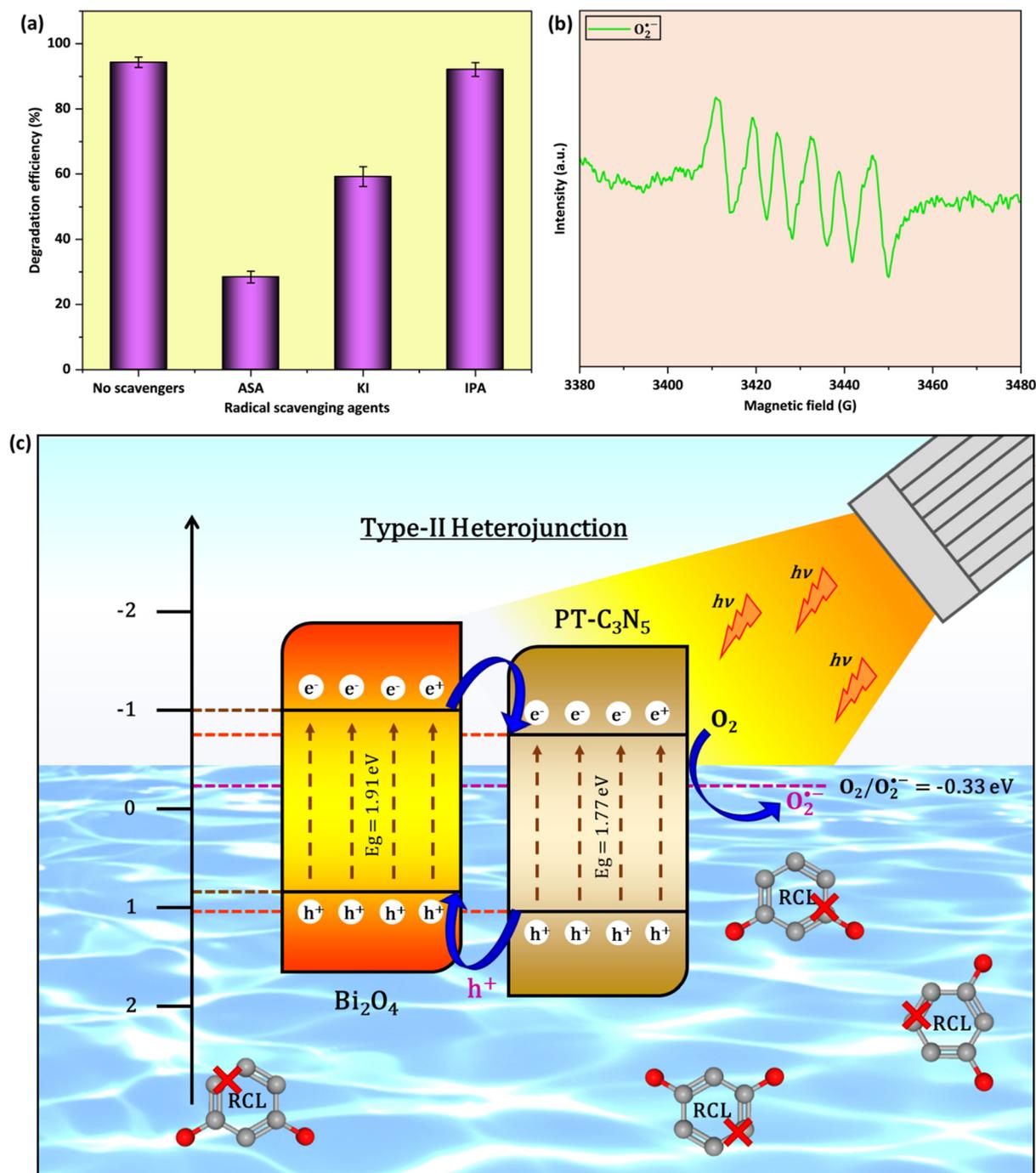
520 | *RSC Appl. Interfaces*, 2026, **3**, 510–526

© 2026 The Author(s). Published by the Royal Society of Chemistry

Fig. 8 (a) Radical capturing experiments using different scavengers in the reaction mixture (BCN-10 dose: 1 g L^{-1}, initial RCL concentration: 5 mg L^{-1}, pH: 7, and temperature: 27 ± 2 °C), (b) EPR spectrum of O$_2$$^{•-}$ and (c) photocatalytic charge transfer mechanism in BCN-10 depicting a type II heterojunction.

H$_2$O, as illustrated in Fig. 9, and numbered in Table S6. The LC-MS/MS technique (as described in Section S2) was employed to determine the TPs and elucidate degradation pathways. In pathway I, the initial radical attack on RCL produced a hydroxylated intermediate, TP1 (m/z = 126). Subsequently, TP1 undergoes ring-opening to form TP2 (m/z = 147). TP2 was then oxidized to low molecular weight aliphatic carboxylic acids, TP3 (m/z = 89) and TP4

(m/z = 43).[95] TP4 can then react with RCL molecules to produce TP5 (m/z = 235), with a relatively larger m/z value (m/z = 235). The aforementioned reaction predominantly occurs at the *ortho* and *para* positions of the RCL molecules.[95] In pathway II, the ring opening of TP1 produces TP6 (m/z = 130), which further oxidizes to produce low molecular weight aliphatic carboxylic acids, TP7 (m/z = 76), TP8 (m/z = 106), and TP9 (m/z = 104).[96]

(a)
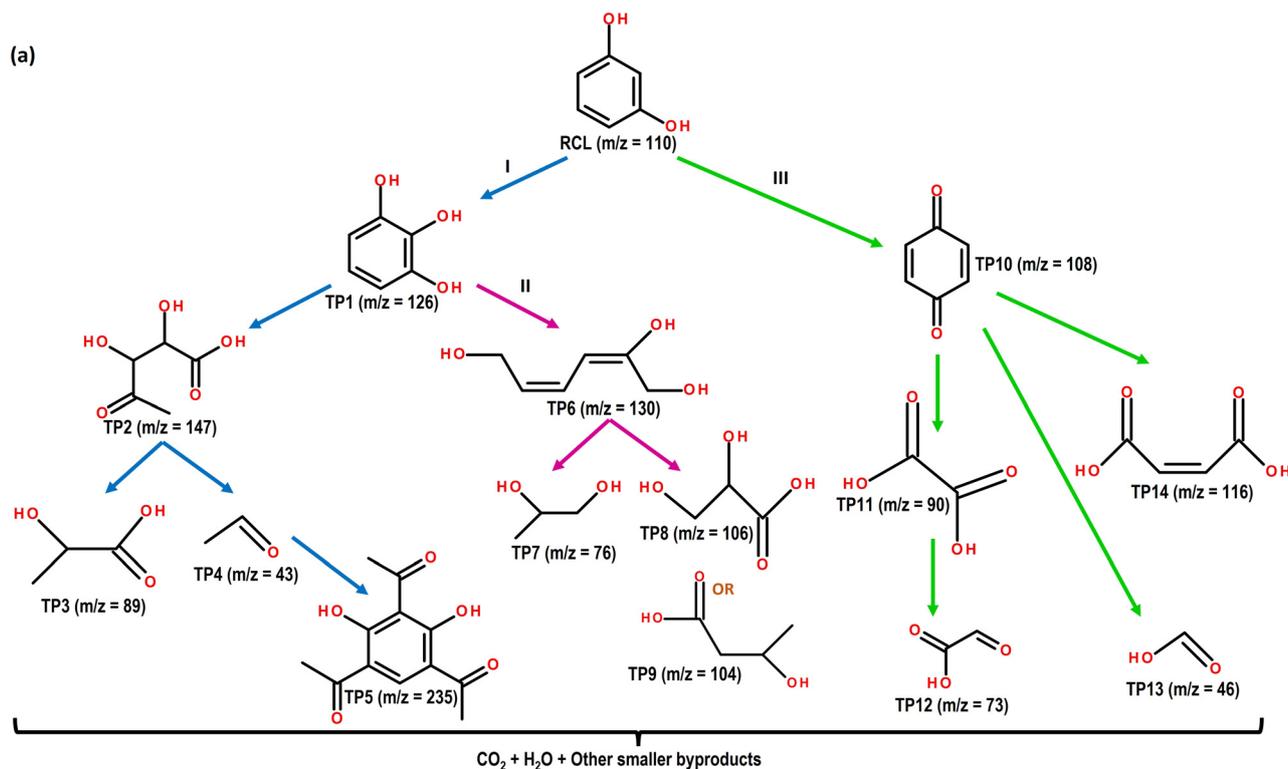
(b)

Parent compound/ Transformation product (TP)	Compound name	Fathead minnow, LC_{50} (96 h)	Daphnia Magna, LC_{50} (48 h)
RCL	*Resorcinol*	38.66	13.88
TP1	*Pyrogallol*	33.63	13.19
TP2	*5-Deoxypent-4-ulosonic acid*	4366.99	1150.79
TP3	*Lactic acid*	2348.07	874.86
TP4	*Acetaldehyde*	221.03	474.72
TP5	*1,1',1''-(2,4-Dihydroxybenzene-1,3,5-triyl)tri(ethan-1-one)*	6.55	26.61
TP6	*(2E, 4E)-penta-2,4-diene-1,2,5-triol*	1254.95	311.12
TP7	*1,2-Propylene glycol*	7237.73	2208.92
TP8	*Glyceric acid*	3580.13	2941.23
TP9	*3-Hydroxybutyric acid*	915.45	804.74
TP10	*1,4-Benzoquinone*	27.82	48.9
TP11	*Oxalic acid*	702.23	1445.45
TP12	*Glyoxylic acid*	211.55	1837.71
TP13	*Formic acid*	601.73	551.98
TP14	*Maleic acid*	187.87	228.79

≤ 1 mg/L	10 mg/L	≥ 100 mg/L

Fig. 9 (a) Degradation pathway of RCL displaying various TPs and (b) *in silico* prediction of ecotoxicity of various TPs of RCL.

In the context of pathway III, RCL undergoes an oxidation reaction, forming TP10 (m/z = 108), and it is further oxidized to TP11 (m/z = 90) and TP12 (m/z = 73).[97] TP13 (m/z = 46) and TP14 (m/z = 116) are produced as a result of the breakdown of TP10.[98] The TPs generated in the aforementioned pathways eventually degrade into low molecular weight aliphatic compounds, ultimately leading to complete mineralization into CO_2 and H_2O.

Furthermore, the ecotoxicity posed by RCL and its TPs was estimated using TEST software. TPs were classified as toxic ($1 < LC_{50} \leq 10$ mg L^{-1}), harmful ($10 < LC_{50} \leq 100$ mg L^{-1}), non-harmful (>100 mg L^{-1}), and highly toxic ($LC_{50} \leq 1$ mg L^{-1}) in accordance with the globally harmonized system of classification and labeling of substances (GHS).[44,99] As displayed in Fig. 9b, RCL was predicted to be a harmful entity; however, after

photocatalytic degradation, most TPs were found to be non-harmful, except for TP1, TP5, and TP10. The prevalence of toxicity in the aforementioned TPs is in accordance with their sustained aromatic, redox-active, and electrophilic nature. Reportedly, TP1 undergoes auto-oxidation in aerated solutions, continuously generating ROS, thereby causing oxidative stress on aquatic creatures.[100] Quinone-type compounds (TP5) can also undergo continuous redox cycling between quinone, and its derivative forms, thereby generating ROS and acting as strong electrophiles that react with biological molecules, causing enzymatic activity inhibition and cellular toxicity.[101] Similar mechanisms have also been reported for TP10 and related quinones, showcasing carcinogenicity and mutagenicity.[102] Although TEST highlights the ecotoxicity potential of individual TPs, it does not consider the combined impacts of TPs in the mixture.

3.8. Assessment of the phytotoxicity potential of the photocatalytically treated RCL solution

A seed germination assay was performed to assess the phytotoxicity risk of the treated effluent containing TPs (Fig. 10a). The RSG and RRG of the control (DI water), untreated (5 mg L^{-1} RCL solution), and photocatalytically treated samples are presented in Fig. 10b and c. Clearly, the RSG and RRG of the control sample were 100%. In comparison, the photocatalytically treated sample exhibited higher values (RSG = 87%; RRG = 94%) than the untreated sample (RSG = 56%; RRG = 39%). This reduction is mainly
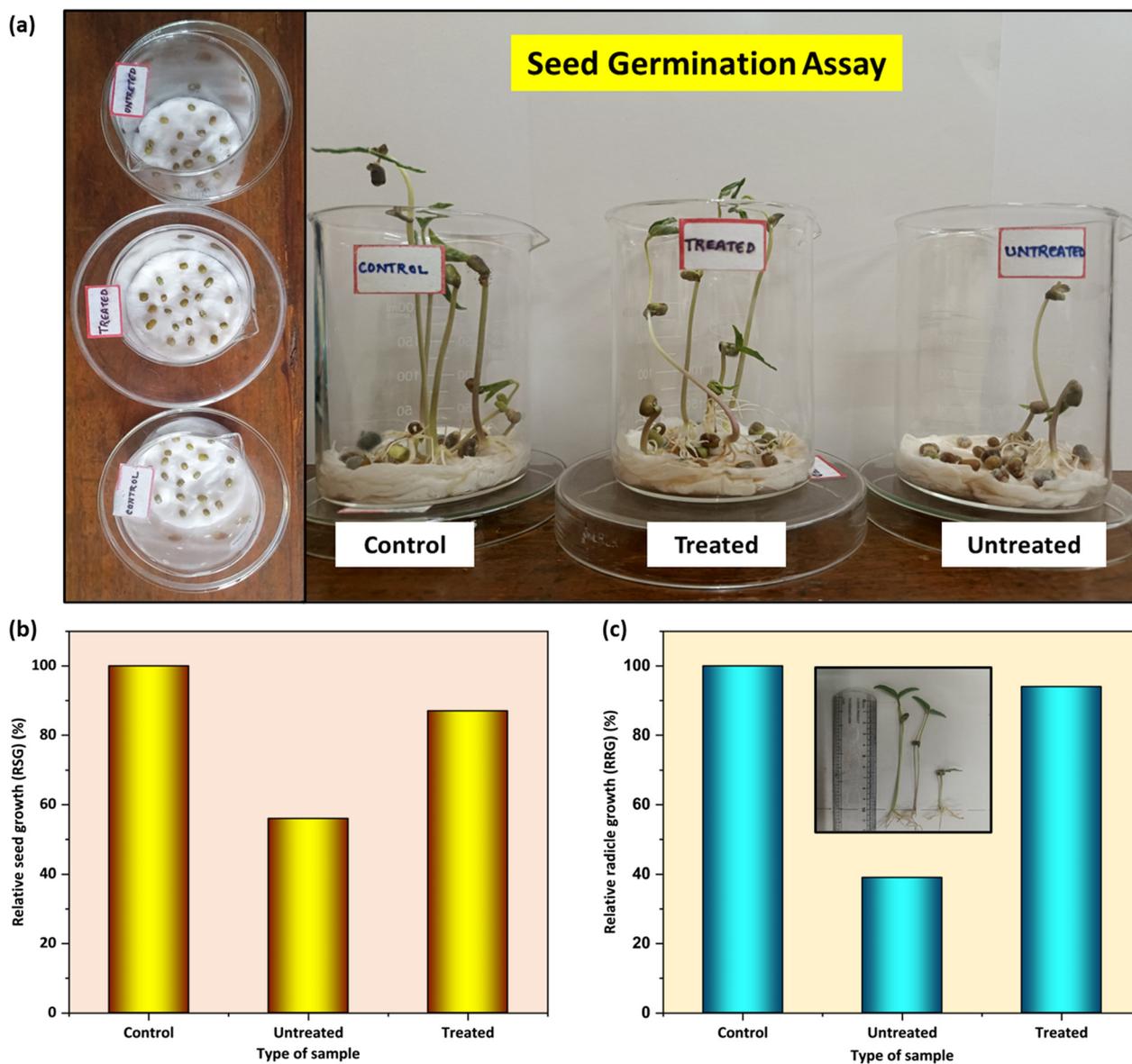

Fig. 10 (a) Seed germination assay using *Vigna radiata* seeds, (b) relative seed growth (RSG), and (c) relative radicle growth (RRG) for treated and untreated samples.

due to the presence of organic pollutants in the untreated sample, which may increase the production of endocellular reactive oxygen species in *Vigna radiata* seeds, inducing oxidative stress. The photocatalytically treated sample was found to have a GI value of ~82%, implying it to be non-phytotoxic.

4. Conclusions

In the present study, a novel type-II heterojunction Bi_2O_4/PT-C_3N_5 photocatalyst was prepared by a facile hydrothermal technique. The morphological assessment revealed quasi-1D rod-like Bi_2O_4 wrapped around 3D block-shaped PT-C_3N_5 with stacked layers. Under optimal conditions (BCN-10 dose: 1 g L^{-1}, initial RCL concentration: 5 mg L^{-1}, pH: 7, and temperature: 27 ± 2 °C), BCN-10 achieved around 94.3% of RCL degradation in 180 min, exhibiting a degradation rate constant of 0.0145 min^{-1}, higher than that of Bi_2O_4 (k = 0.0054 min^{-1}) and PT-C_3N_5 (k = 0.0015 min^{-1}). This could be associated with the improved visible light absorption potential resulting from the narrowing of the energy bandgap and the reduction of charge carrier recombination due to the creation of an interfacial heterojunction between constituent materials in BCN-10. The presence of HCO_3^- ions and humic acid had the most detrimental effect on RCL degradation, reducing the degradation efficacy to 66.8% and 29.6%, respectively. The extent of Bi-leaching at the end of the reaction period was negligible, indicating BCN-10 to be chemically stable. The BCN-10 photocatalyst showed reusability potential up to 5 cycles with a reduction of ~12% in RCL degradation. As proven by the radical capturing experiment, $O_2^{\cdot-}$ was the main active species participating in RCL degradation, followed by h^+. The co-occurrence of other ECs and real water matrices showed an adverse impact on RCL degradation, possibly due to the simultaneous consumption of active radicals and competitive adsorption of inorganic ions on BCN-10 active sites, respectively. The *in silico* prediction of TPs generated during RCL degradation indicated that they were mostly non-toxic. Further, it was confirmed that the treated RCL solution was devoid of phytotoxicity.

Author contributions

Adarsh Singh: writing – original draft, validation, methodology, investigation, formal analysis, data curation, conceptualization. Balbir: writing – original draft, validation, methodology, investigation, formal analysis, data curation, conceptualization. Suneel Kumar Srivastava: writing – review & editing, visualization, supervision, methodology, conceptualization. Amit Bhatnagar: writing – review & editing, visualization, supervision, methodology, conceptualization. Ashok Kumar Gupta: writing – review & editing, visualization, supervision, methodology, conceptualization.

Conflicts of interest

There are no conflicts of interest to declare.

Data availability

The data that support the findings of this study will be made available from the corresponding author upon reasonable request.

Supplementary information (SI) is available. See DOI: https://doi.org/10.1039/d5lf00338e.

References

1 S. Keerthanan, C. Jayasinghe, J. K. Biswas and M. Vithanage, *Crit. Rev. Environ. Sci. Technol.*, 2021, **51**, 1221–1258.

2 A. J. Ebele, T. Oluseyi, D. S. Drage, S. Harrad and M. Abou-Elwafa Abdallah, *Emerging Contam.*, 2020, **6**, 124–132.

3 J. Fick, H. Söderström, R. H. Lindberg, C. Phan, M. Tysklind and D. G. J. Larsson, *Environ. Toxicol. Chem.*, 2009, **28**, 2522–2527.

4 X.-Z. Min, Z.-F. Zhang, X.-M. Lu, J.-C. Chen, W.-L. Ma, L.-Y. Liu, W.-L. Li, Y.-F. Li and R. Kallenborn, *Sci. Total Environ.*, 2024, **924**, 171589.

5 D. Wu, Q. Sui, X. Yu, W. Zhao, Q. Li, D. Fatta-Kassinos and S. Lyu, *Sci. Total Environ.*, 2021, **753**, 141653.

6 A. Chakraborty, S. Adhikary, S. Bhattacharya, S. Dutta, S. Chatterjee, D. Banerjee, A. Ganguly and P. Rajak, *ACS Chem. Health Saf.*, 2023, **30**, 362–388.

7 A. J. Ebele, M. Abou-Elwafa Abdallah and S. Harrad, *Emerging Contam.*, 2017, **3**, 1–16.

8 R. A. W. F. Aguilar, U. R. Charrondiere, B. Dusemund, P. Galtier, J. Gilbert, D. M. Gott, S. Grilli, R. Guertler, J. Koenig, C. Lambré, J.-C. Larsen, J.-C. Leblanc, A. Mortensen, D. Parent-Massin, I. Pratt, I. M. C. M. Rietjens, I. Stankovic, P. Tobback and T. Verguieva, *EFSA J.*, 2010, **8**, 1411.

9 A. Ballesteros-Gómez, N. Van den Eede and A. Covaci, *Environ. Sci. Technol.*, 2015, **49**, 3897–3904.

10 S. Hahn, J. Kielhorn, J. Koppenhöfer, A. Wibbertmann and I. Mangelsdorf, *Resorcinol*, WHO, 2006, https://iris.who.int/server/api/core/bitstreams/30ff8258-12a4-4433-bd50-071425bc48ef/content.

11 B. S. Lynch, E. S. Delzell and D. H. Bechtel, *Regul. Toxicol. Pharmacol.*, 2002, **36**, 198–210.

12 R. C. Cooksey, E. Gaitan, R. H. Lindsay, J. B. Hill and K. Kelly, *Org. Geochem.*, 1985, **8**, 77–80.

13 A. Singh, A. Majumder, D. Saidulu, A. Bhattacharya, A. Bhatnagar and A. K. Gupta, *J. Environ. Manage.*, 2024, **354**, 120339.

14 V. K. Parida, M. V. Lincy Gnanaguru, S. K. Srivastava, S. Chowdhury and A. K. Gupta, *Environ. Sci.: Water Res. Technol.*, 2024, **10**, 3319–3338.

15 S. S. Thind, M. Paul, J. B. Hayden, A. Joshi, D. Goodlett and J. S. McIndoe, *Ind. Chem. Mater.*, 2023, **1**, 431–442.

16 A. Singh and A. K. Gupta, *Environ. Sci.: Nano*, 2026, **13**, 563–581.

17 C. Karthikeyan, P. Arunachalam, K. Ramachandran, A. M. Al-Mayouf and S. Karuppuchamy, *J. Alloys Compd.*, 2020, **828**, 154281.

18 S. K. Srivastava, *RSC Appl. Interfaces*, 2024, **1**, 340–429.

19 A. Hameed, V. Gombac, T. Montini, L. Felisari and P. Fornasiero, *Chem. Phys. Lett.*, 2009, **483**, 254–261.

20 D. Chen, S. Wu, J. Fang, S. Lu, G. Zhou, W. Feng, F. Yang, Y. Chen and Z. Fang, *Sep. Purif. Technol.*, 2018, **193**, 232–241.

21 C. Li, Y. Ma, S. Zheng, C. Hu, F. Qin, L. Wei, C. Zhang, S. Duo and Q. Hu, *J. Phys. Chem. Solids*, 2020, **140**, 109376.

22 Y. Xing, F. Tian, D. Wu, X. Yong, X. Jin and G. Ni, *Inorg. Chem. Commun.*, 2022, **143**, 109763.

23 D. Xia and I. M. C. Lo, *Water Res.*, 2016, **100**, 393–404.

24 H. Y. Wang, Z. S. Liu, Y. L. Zhao, J. N. Niu and P. Z. Feng, *Mater. Res. Bull.*, 2017, **89**, 253–262.

25 S. Hernández, G. Saracco, G. Barbero and A. L. Alexe-Ionescu, *J. Electroanal. Chem.*, 2017, **799**, 481–486.

26 S. K K, A. Singh, S. K. Srivastava, A. Bhattacharya, A. Bhatnagar and A. K. Gupta, *Dalton Trans.*, 2025, **54**, 2403–2420.

27 M. Zhou, J. Bao, Y. Xu, J. Zhang, J. Xie, M. Guan, C. Wang, L. Wen, Y. Lei and Y. Xie, *ACS Nano*, 2014, **8**, 7088–7098.

28 X. Liu, Y. Liu, X. Guo, B. Tao, X. Ma, S. Cheng, N. Tian, G. Liu, Q. Wu, V. Q. Bui, K. K. Saxena, S. G. Ramaraj, J. Liu, F. Zhang and Y. Zhu, *Ind. Chem. Mater.*, 2025, **3**, 191–202.

29 V. K. Parida, S. K. Srivastava, S. Chowdhury and A. K. Gupta, *Chem. Eng. J.*, 2023, **472**, 144969.

30 A. Rawat, S. K. Srivastava, C. S. Tiwary and A. K. Gupta, *J. Mater. Chem. A*, 2025, **13**, 1271–1286.

31 H. Cheng, J. Hou, O. Takeda, X.-M. Guo and H. Zhu, *J. Mater. Chem. A*, 2015, **3**, 11006–11013.

32 Z. Zhao, Y. Sun and F. Dong, *Nanoscale*, 2015, **7**, 15–37.

33 Z. Zhao, Y. Sun, F. Dong, Y. Zhang and H. Zhao, *RSC Adv.*, 2015, **5**, 39549–39556.

34 Y. Li, X. Li, H. Zhang, J. Fan and Q. Xiang, *J. Mater. Sci. Technol.*, 2020, **56**, 69–88.

35 W. Yan, L. Yan and C. Jing, *Appl. Catal., B*, 2019, **244**, 475–485.

36 S. C. Yan, Z. S. Li and Z. G. Zou, *Langmuir*, 2009, **25**, 10397–10401.

37 S. Ng, J. J. Foo and W. Ong, *InfoMat*, 2022, **4**, e12279.

38 L. Lin, Z. Yu and X. Wang, *Angew. Chem.*, 2019, **131**, 6225–6236.

39 Y. Shao, X. Hao, S. Lu and Z. Jin, *Chem. Eng. J.*, 2023, **454**, 140123.

40 P. Kumar, E. Vahidzadeh, U. K. Thakur, P. Kar, K. M. Alam, A. Goswami, N. Mahdi, K. Cui, G. M. Bernard, V. K. Michaelis and K. Shankar, *J. Am. Chem. Soc.*, 2019, **141**, 5415–5436.

41 I. Y. Kim, S. Kim, X. Jin, S. Premkumar, G. Chandra, N. Lee, G. P. Mane, S. Hwang, S. Umapathy and A. Vinu, *Angew. Chem.*, 2018, **130**, 17381–17386.

42 Z. Li, W. Zeng, M. Li, J. Zheng, X. Fang and M. Lin, *Macromol. Rapid Commun.*, 2021, **42**, 2100577.

43 S.-F. Ng, J. J. Foo and W.-J. Ong, *Mater. Horiz.*, 2024, **11**, 408–418.

44 A. Singh, A. Bhatnagar and A. K. Gupta, *J. Environ. Chem. Eng.*, 2024, **12**, 114192.

45 M. S. I. Nasri, M. F. R. Samsudin, A. A. Tahir and S. Sufian, *Energies*, 2022, **15**, 955.

46 S. Wang, L. Chen, X. Zhao, J. Zhang, Z. Ao, W. Liu, H. Wu, L. Shi, Y. Yin, X. Xu, C. Zhao, X. Duan, S. Wang and H. Sun, *Appl. Catal., B*, 2020, **278**, 119312.

47 V. T. Vu, S. Bartling, T. Peppel, H. Lund, C. Kreyenschulte, J. Rabeah, N. G. Moustakas, A.-E. Surkus, H. D. Ta and N. Steinfeldt, *Colloids Surf., A*, 2020, **589**, 124383.

48 G. Yu, H. Zhao, C. Xing, L. Guo and X. Li, *Catal. Sci. Technol.*, 2021, **11**, 5349–5359.

49 W. Wang, X. Chen, G. Liu, Z. Shen, D. Xia, P. K. Wong and J. C. Yu, *Appl. Catal., B*, 2015, **176–177**, 444–453.

50 R. Shyam, A. Kumar, S. Pal and R. Prakash, *Electrochim. Acta*, 2024, **496**, 144485.

51 V. K. Yadav and T. Das, *Phys. Chem. Chem. Phys.*, 2021, **23**, 13612–13622.

52 W. Sun, X. Bao, H. Wang, Z. Liu, Z. Tian, H. Li and X. Yuan, *Appl. Surf. Sci.*, 2024, **642**, 158655.

53 B. Chai, X. Liao, F. Song and H. Zhou, *Dalton Trans.*, 2014, **43**, 982–989.

54 N. Li, Y. Tian, J. Zhao, J. Zhang, W. Zuo, L. Kong and H. Cui, *Chem. Eng. J.*, 2018, **352**, 412–422.

55 W. Liu, Q. Kang, L. Wang, L. Wen and Z. Li, *Environ. Sci. Pollut. Res.*, 2022, **29**, 51989–52002.

56 S. S. Rojas, J. E. De Souza, M. R. B. Andreeta and A. C. Hernandes, *J. Non-Cryst. Solids*, 2010, **356**, 2942–2946.

57 M. Sadhukhan and S. Barman, *J. Mater. Chem. A*, 2013, **1**, 2752.

58 R. Iordanova, M. Milanova, L. Aleksandrov and A. Khanna, *J. Non-Cryst. Solids*, 2018, **481**, 254–259.

59 H. H. Yang, K.-Y. Hsiao, F.-Y. Liu, C.-C. Chen and I.-C. Chen, *J. Phys. Chem. C*, 2024, **128**, 563–570.

60 E. Mosquera, R. S. Katiyar and C. Marin, *Vib. Spectrosc.*, 2019, **100**, 191–194.

61 V. N. Denisov, B. N. Mavrin, V. B. Podobedov, I. V. Alexandrov, A. B. Bykov, A. F. Goncharov, O. K. Mel'nikov and N. I. Romanova, *Solid State Commun.*, 1989, **70**, 885–888.

62 A. Hamrouni, M. Moussa, N. Fessi, L. Palmisano, R. Ceccato, A. Rayes and F. Parrino, *Nanomaterials*, 2023, **13**, 2742.

63 J. Li, Y. Li, G. Zhang, H. Huang and X. Wu, *ACS Appl. Mater. Interfaces*, 2019, **11**, 7112–7122.

64 Y. Tang, X. Wang, J. Chen, X. Wang, D. Wang and Z. Mao, *Carbon*, 2020, **168**, 458–467.

65 S. Deka, M. B. Devi, M. R. Khan, Keerthana, A. Venimadhav and B. Choudhury, *ACS Appl. Nano Mater.*, 2022, **5**, 10724–10734.

© 2026 The Author(s). Published by the Royal Society of Chemistry

RSC Appl. Interfaces, 2026, **3**, 510–526 | **525**

66   M. Qin, K. Jin, X. Li, R. Wang, Y. Zhao and H. Wang, *New J. Chem.*, 2022, **46**, 12410–12418.

67   S. Arunpandiyan, A. Raja, S. Vinoth, A. Pandikumar and A. Arivarasan, *New J. Chem.*, 2021, **45**, 12808–12817.

68   V. D. Mote, S. D. Lokhande, L. H. Kathwate, M. B. Awale and Y. Sudake, *Mater. Sci. Eng., B*, 2023, **289**, 116254.

69   Y. S. Zou, Q. M. Wang, H. Du, G. H. Song, J. Q. Xiao, J. Gong, C. Sun and L. S. Wen, *Appl. Surf. Sci.*, 2005, **241**, 295–302.

70   S. Kaushal, V. Kumari and P. P. Singh, *Environ. Sci. Pollut. Res.*, 2023, **30**, 65602–65617.

71   T. Kokulnathan, R. Vishnuraj, T.-J. Wang and B. Pullithadathil, *Appl. Surf. Sci.*, 2022, **604**, 154474.

72   S. Kang, L. Zhang, C. Yin, Y. Li, L. Cui and Y. Wang, *Appl. Catal., B*, 2017, **211**, 266–274.

73   Y. Zhou, L. Zhang, W. Huang, Q. Kong, X. Fan, M. Wang and J. Shi, *Carbon*, 2016, **99**, 111–117.

74   K. Kalidasan, S. Mallapur, P. Vishwa and S. Kandaiah, *Ind. Eng. Chem. Res.*, 2022, **61**, 16673–16688.

75   S. Li, C. Wang, Y. Liu, B. Xue, W. Jiang, Y. Liu, L. Mo and X. Chen, *Chem. Eng. J.*, 2021, **415**, 128991.

76   J. Yao, L. Huang, Y. Li, M. Zhu, S. Liu, S. Shu, L. Huang and X. Wu, *Ceram. Int.*, 2023, **49**, 19422–19433.

77   A. Ataei, A. Mehrizad and K. Zare, *J. Mol. Liq.*, 2021, **328**, 115476.

78   Y. Li, X. Li, S. Wang, S. Tan, Y. Xia, J. Shi, W. Chen and L. Gao, *Colloids Surf., A*, 2022, **643**, 128806.

79   M. Vino, L. Gnanaguru, M. Naushad, T. Tatarchuk and M. M. Ghangrekar, *Environ. Sci. Pollut. Res.*, 2023, **30**, 78537–78553.

80   A. Singh, A. Bhatnagar and A. K. Gupta, *Sep. Purif. Technol.*, 2025, 132176.

81   F. Chen, Q. Yang, X. Li, G. Zeng and D. Wang, *Appl. Catal., B*, 2017, **200**, 330–342.

82   M. A. Álvarez, F. Orellana-García, M. V. López-Ramón, J. Rivera-Utrilla and M. Sánchez-Polo, *Arabian J. Chem.*, 2018, **11**, 564–572.

83   Y. Shen and C. Lin, *Water Environ. Res.*, 2003, **75**, 54–60.

84   F. Peng, R. Yin, Y. Liao, X. Xie, J. Sun, D. Xia and C. He, *Chem. Eng. J.*, 2020, **392**, 123818.

85   D. E. Santiago, J. Araña, O. González-Díaz, M. E. Alemán-Dominguez, A. C. Acosta-Dacal, C. Fernandez-Rodríguez, J.

Pérez-Peña and J. M. Doña-Rodríguez, *Appl. Catal., B*, 2014, **156–157**, 284–292.

86   R. A. Burns, J. C. Crittenden, D. W. Hand, V. H. Selzer, L. L. Sutter and S. R. Salman, *J. Environ. Eng.*, 1999, **125**, 77–85.

87   F. Orellana-García, M. A. Álvarez, M. V. López-Ramón, J. Rivera-Utrilla and M. Sánchez-Polo, *Chem. Eng. J.*, 2015, **267**, 182–190.

88   F. Chen, J. Li, L. Xia, J. Wang, S. Chen, Y. Zhang, J. Bai, L. Li, T. Zhou, M. Rahim, Q. Xu and B. Zhou, *Appl. Catal., B*, 2020, **277**, 119227.

89   D. Luo, P. Zhu, M. Duan, M. Liu, H. Lu and Z. Huang, *Sep. Purif. Technol.*, 2023, **311**, 123287.

90   D. Awfa, M. Ateia, M. Fujii and C. Yoshimura, *Water Res.*, 2020, **174**, 115643.

91   V. M. Chakachaka, C. S. Tshangana, B. B. Mamba and A. A. Muleja, *Membranes*, 2023, **13**, 827.

92   D. C. A. Gowland, N. Robertson and E. Chatzisymeon, *Water*, 2021, **13**, 288.

93   E. M. Khudhair, S. H. Ammar, S. Z. Al-Najjar, S. M. Al-Jubouri, A. S. Mahdi and Z. H. Jabbar, *Mater. Lett.*, 2023, **347**, 134599.

94   A. Maulidya, Y. Yulizar, R. Bakri, D. O. B. Apriandanu and R. M. Surya, *Ceram. Int.*, 2022, **48**, 29523–29532.

95   M. Sun, Y. Bi, T. Yan, Y. Zhang, T. Wu, Y. Shao, D. Wei and B. Du, *J. Hazard. Mater.*, 2018, **358**, 20–32.

96   S. Lam, J. Sin, A. Z. Abdullah and A. R. Mohamed, *Environ. Technol.*, 2013, **34**, 1097–1106.

97   Z. Hu, W. Zhang, Y. Zhong, Q. Duan, Z. Liu, B. Wang, L. Chen, X. Wang and X. Zhang, *ACS Appl. Nano Mater.*, 2024, **7**, 20653–20664.

98   C. Hou, L. Wang, W. Zhang, Z. Zhu, S. Lu, F. Zou and C. Wang, *ACS Appl. Mater. Interfaces*, 2023, **15**, 23124–23135.

99   United Nations, *Globally Harmonized System of Classification and Labelling of Chemicals (GHS)*, New York, Geneva, 2011.

100   S. Marklund and G. Marklund, *Eur. J. Biochem.*, 1974, **47**, 469–474.

101   J. L. Bolton and T. Dunlap, *Chem. Res. Toxicol.*, 2017, **30**, 13–37.

102   S. S. Lau, B. A. Hill, R. J. Highet and T. J. Monks, *Mol. Pharmacol.*, 1988, **34**, 769–778.